

Seismogenic Structure and Rupture Characteristics of the 2023 Ms 4.9 Earthquake in Xingwen (Sichuan, China)

Guanyu Mao¹, Yingwen Zhao^{1*}, Guoyan Jiang^{1*}, Haoran Dong², Quanshu Zhao¹, Jian Xu², Junlun Li²

¹School of Earth and Space Science and Technology, Wuhan University, Wuhan 430072, China;

² School of Earth and Space Sciences, University of Science and Technology of China, Hefei 230026, China;

Correspondence to: Y.W.Zhao, yingwenzh@whu.edu.cn and G.Y.Jiang, gyjiang@whu.edu.cn

Key Points:

- 1. The Xingwen earthquake caused prominent surface deformation with the maximum line-of-sight displacement of ~3 cm.**
- 2. The relocation results of aftershocks indicated the seismogenic fault dipping to east at an angle of 23.3°.**
- 3. Major slip of the Xingwen earthquake occurred below the shale gas formation with a peak value of 11.58 cm.**

Abstract

On 4 May 2023, a Ms 4.9 earthquake struck Xingwen, Sichuan, China. Although moderate in magnitude, the event posed potential threats to nearby shale gas production and residents. However, the seismogenic fault and rupture characteristics remained unclear. Here, we jointly use InSAR observations and seismological data to determine the source parameters and fault geometry. Eighteen Sentinel-1A SAR images from two ascending orbits were processed using the D-InSAR technique, with noise reduced through multi-interferogram stacking. The derived co-seismic deformation field indicates a thrust-dominated rupture with a maximum line-of-sight displacement of about 3 cm. Using a combination of multi-start adaptive Gauss–Newton nonlinear inversion and bounded least-squares linear inversion, we resolved the fault plane geometry and slip distribution. Together with aftershock analysis via Principal Component Analysis (PCA), the seismogenic fault was identified as an east-dipping blind thrust fault (strike 345° , dip 23.3°), with slip concentrated at depths of 2–4 km. The released seismic moment (4.38×10^{16} N·m, Mw 5.0) reveals a shallow rupture. This study clarifies the rupture mechanism of the Xingwen earthquake and highlights the value of integrating geodetic and seismological methods for fault identification and seismic risk assessment in shale gas regions.

Keywords

The Ms 4.9 Xingwen earthquake; InSAR; Geodetic inversion; Seismicity relocation; Seismogenic structure.

1 Introduction

On May 4, 2023, a Ms 4.9 earthquake struck Xingwen, Sichuan, China, causing regional concern due to its proximity to shale gas production areas. In the same period, three smaller earthquakes with magnitudes of Ms 4.0, Ms 4.5, and Ms 4.3 (Figure 1b) also occurred nearby, but their impacts were much weaker. As the largest event in this sequence, the Ms 4.9 earthquake is considered to be primarily responsible for the observed surface deformation and potential seismic hazard in the region.

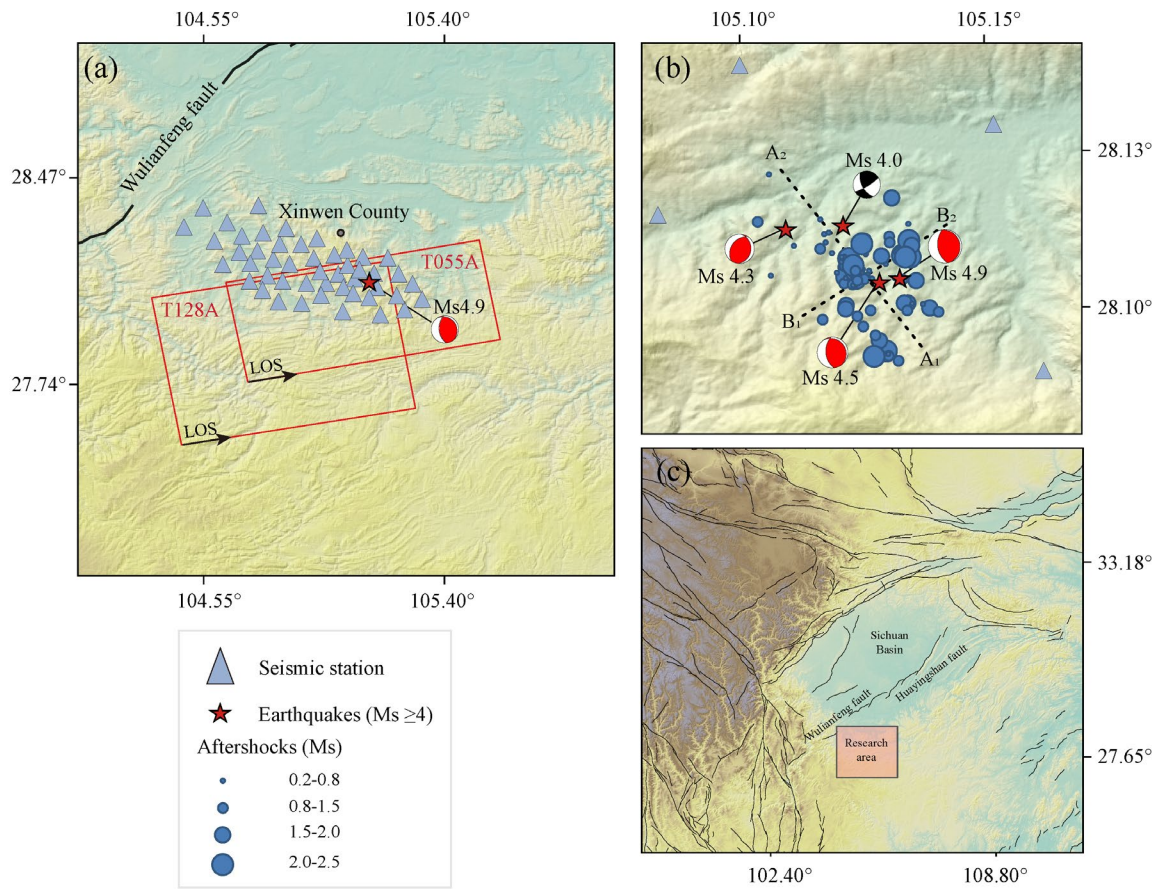


Figure 1. Seismogeological setting of the 2023 Ms 4.9 Xingwen earthquake. (a) The red rectangle outlines the coverage of Sentinel-1 satellite images from two orbits. Black arrows indicate the satellite's line-of-sight (LOS) direction. Blue triangles mark the deployed real-time short-period nodal seismometers. (b) Earthquake locations within 6.57 hours after the Ms 4.9 event. Line A1A2 depicts the fault derived from PCA fitting, while B1B2 is an auxiliary line perpendicular to A1A2. Red pentagram denotes the epicenters of the 4 earthquakes, Ms ≥ 4.0 in the sequence, with focal mechanism solutions (beach balls) plotted for each (Kong LZ et al., 2024). (c) Regional geological setting of the Xingwen area. Black solid lines represent nearby faults and fractures.

Previous research by Kong LZ et al.(2024) analyzed broadband waveform data from permanent stations within 300 km of the epicenter and derived focal mechanism solutions using the CAP method. Their results suggested that the Ms 4.9 earthquake was a thrust-slip event, with nodal planes oriented mainly in the NW–SE and NE–SW directions. However, the study did not identify the seismogenic fault or clarify the detailed rupture characteristics. Moreover, as no significant surface rupture was detected, it was inferred that the event may have originated from blind thrust structures controlling regional folds in the basin. Consequently, the source geometry and the specific fault responsible for the Xingwen earthquake sequence remain uncertain.

To address these issues, this study employs geodetic observations to investigate the seismogenic structure and rupture process of the Ms 4.9 earthquake. Eighteen ascending-track Sentinel-1A SAR images were processed using the D-InSAR technique to derive the co-seismic deformation, with noise suppressed through multi-interferogram stacking. By combining nonlinear and linear inversion approaches, we determined the fault geometry and slip distribution. Furthermore, by integrating the relocated microseismic events analyzed through Principal Component Analysis (PCA), we identified the actual seismogenic fault and revealed the rupture characteristics of the Xingwen Ms 4.9 earthquake.

2 Geological Background

The southern Sichuan shale gas development area, located in the southeastern margin of the Sichuan Basin on the northwestern edge of the Yangtze Block, has long exhibited relatively low seismic activity and overall structural stability. The region lies within the southeastern Sichuan fold belt, where NE–SW-trending folds and thrust faults are well developed. The Huayingshan and Wulianfeng faults serve as the main tectonic boundaries, controlling the regional deformation pattern along the southern margin of the basin (Figure 1c).

Since the initiation of shale gas exploration in the Changning area in 2008, and especially after the large-scale implementation of horizontal well hydraulic fracturing in 2014, local seismic

activity has increased significantly. Within the Changning shale gas field, a key production zone of the Sichuan basin, a growing number of small-to-moderate earthquakes have shown strong spatial and temporal correlations with industrial stimulation activities, suggesting that human operations have become an important factor influencing regional seismicity (Miao SY et al., 2024).

The Xingwen earthquake sequence in May 2023 occurred within the Changning shale gas field, where intensive industrial operations are concentrated. Within a 5 km radius of the seismic zone, ten hydraulic fracturing well pads were active before May 2023, including two located within 3 km that were closely correlated in time and space with the four $M_s \geq 4.0$ seismic events. Understanding the seismogenic fault and rupture characteristics of the largest $M_s 4.9$ event is therefore crucial for clarifying the mechanisms of induced or triggered seismicity in the southern Sichuan shale gas region.

3 InSAR-measured Co-seismic Deformation

To capture the coseismic deformation associated with the Xingwen earthquake sequence, two ascending Sentinel-1A tracks (055 and 128) were selected, providing good spatial coverage across the study area (Figure 1a). For each track, three pre- and three post-earthquake SAR images were acquired, forming nine interferometric pairs per track. Standard D-InSAR processing was conducted using the software GAMMA (Werner et al., 2000), producing a total of 18 coseismic interferograms (Tian X & Liao MS, 2013; Zhao YW et al., 2023). Although the observation periods covered all four $M_s \geq 4.0$ events, the detected surface deformation was primarily induced by the $M_s 4.9$ earthquake, which released significantly greater energy than the other events.

Initial D-InSAR interferograms revealed evident deformation signals near the epicentral area but were heavily contaminated by turbulent atmospheric noise and decorrelation effects, particularly in low-coherence regions. A polynomial model with a linear DEM term (Doin et al., 2009) was applied to reduce orbital errors and topography-correlated atmospheric noise. However, due to the small spatial scale of the deformation ($<10 \times 10$ km), existing atmospheric correction models with

coarse spatial resolution (\sim 20 km; Zhao YW et al., 2023) were insufficient for mitigating small-scale turbulence (Wang S et al., 2022). As a result, the deformation fringes were partially fragmented, limiting the precision of the coseismic signal extraction.

To further suppress noise and enhance deformation clarity, a multi-interferogram stacking approach (Jiang GY et al., 2018; Luo H et al., 2021; Zhao YW et al., 2025) was applied. Interferograms with varying temporal baselines were averaged after masking low-coherence regions. A unified mask was adopted for each track to ensure spatial consistency: high-coherence interferograms (20230425–20230507 for Track 055, and 20230430–20230512 for Track 128) defined the near-field mask with a coherence threshold of 0.9, while far-field masks were determined from lower-coherence interferograms to exclude large errors. Interferograms with coherence coverage below 50% were discarded, and finally two high-quality interferograms per track were selected for stacking (Figure 2a and 2b). This strategy maximized preservation of near-field deformation while minimizing residual noise.

The stacked results (Figure 2c) show a substantial reduction in noise within non-deformation areas, where the standard deviation decreased by nearly 50% on average. The resulting LOS (Line of Sight) deformation fields reveal surface displacements of up to \sim 3 cm, concentrated within a NE–SW-trending elliptical zone. The epicenter of the Ms 4.9 event lies at the east-central part of the deformation area, which overall exhibits uplift (LOS shortening), consistent with a thrust-faulting mechanism. To facilitate inversion, an improved quadtree downsampling method incorporating topological analysis (Wang S et al., 2022) was applied, yielding 330 and 261 LOS observations for tracks 055 and 128 (Figure 2c), respectively. These refined datasets provide a reliable basis for subsequent fault geometry and slip distribution inversions.

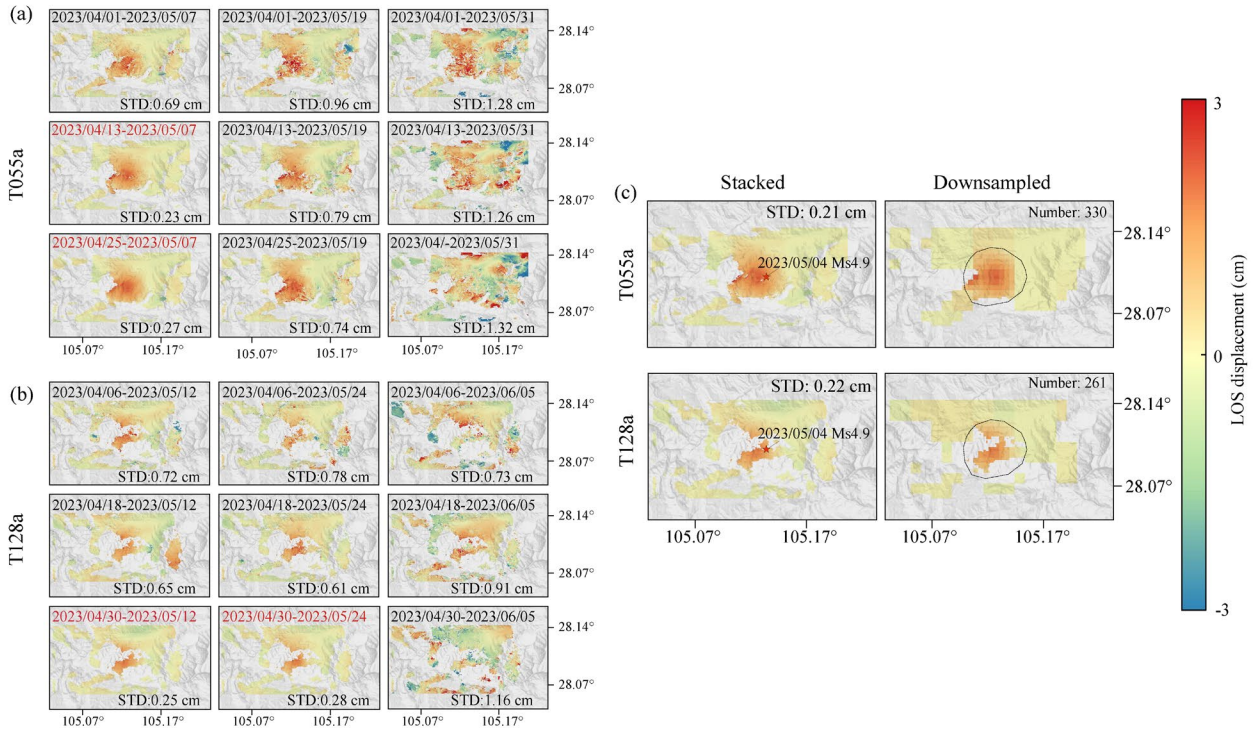


Figure 2. Coseismic InSAR observations. (a) Interferograms from Track 055a. Red label indicates the two interferograms with highest coherence. (b) Interferograms from Track 128a. Red label indicates the two interferograms with highest coherence. (c) Stacked results and downsampled results.

4 InSAR inversions for slip model

4.1 Nonlinear Inversion for Fault Geometry

To determine the source parameters of the seismogenic fault, we conducted nonlinear inversions using the multi-start adaptive Gauss–Newton method (Zhao YW and Xu CJ, 2020). This algorithm adaptively adjusts the number and range of initial parameter values through non-uniform sampling, enabling an efficient global search and reducing the risk of local convergence. Two candidate fault geometries—east-dipping and west-dipping—were constructed based on the two nodal planes of the focal mechanism solution (Kong LZ et al., 2024). The Okada (1992) rectangular dislocation model in a homogeneous elastic half-space was used to calculate Green’s functions, and weighting factors were assigned according to the standard deviation of the LOS observations from the ascending and descending tracks.

In practice, only Sentinel-1A ascending track data were available for the study area, causing the strike angle to converge toward the sampling boundary during the initial inversion. To constrain the model, the strike angles were fixed at 345° and 171° , respectively, following the CAP-derived focal mechanism (Kong LZ et al., 2024), and the nonlinear inversion was repeated under these fixed-strike conditions. The final fault parameter solutions obtained from the optimized inversion are presented in Table 1.

Based on the covariance matrix calculated from the inverted source parameters, the correlations and uncertainties among the fault geometry parameters were quantitatively assessed. The confidence ellipses of the two nodal plane models (Figure 3) were then derived from these covariances, providing a visual representation of the parameter confidence intervals. The results indicate that all source parameters were well constrained, except for a pronounced trade-off between fault length and slip amount. Overall, the inversion yielded a reliable estimation of the

fault geometry, providing a robust foundation for further analysis of source characteristics and tectonic implications.

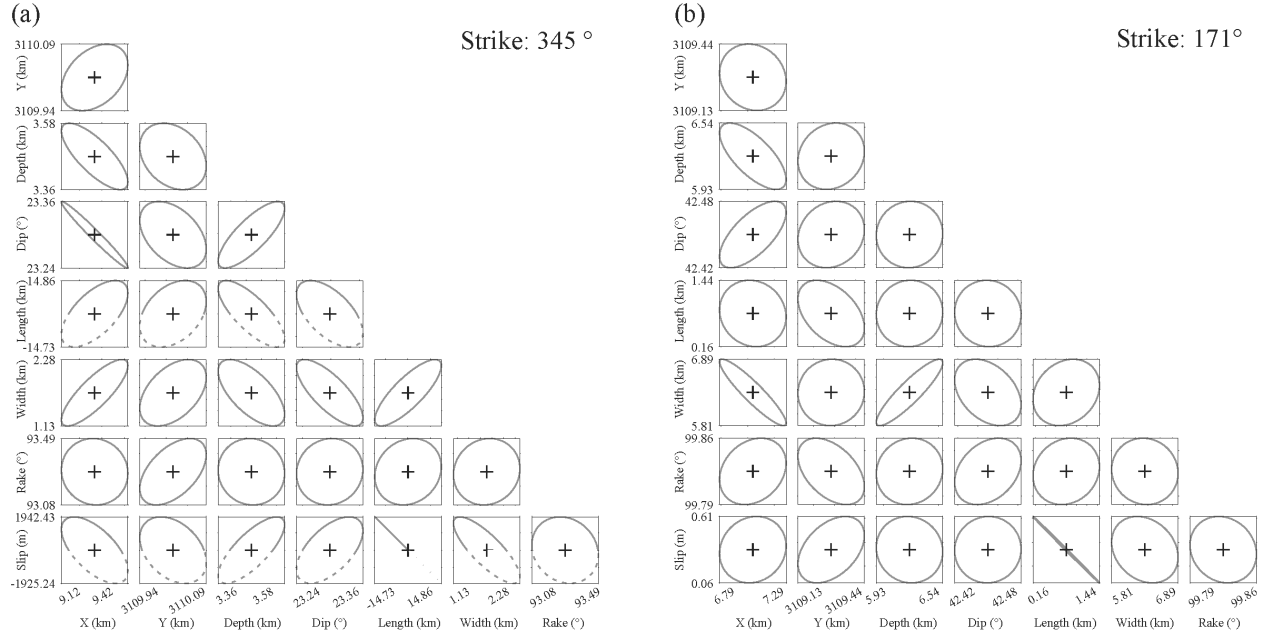


Figure 3. The confidence ellipses of the two nodal plane models. (a) The confidence ellipses of the fault model with strike angle at 345° . (b) The confidence ellipses of the fault model with strike angle at 171° .

Table 1. Final result of fault parameter. In our result, longitude, latitude and depth refer to the center coordinates and bottom depth of the fault plane.

Epicenter		Depth (km)	Nodal Plane 1			Nodal Plane 2			Length (km)	Width (km)	Magnitude (Mw)	Source
Longitude (°)	Latitude (°)		Strike (°)	Dip (°)	Rake (°)	Strike (°)	Dip (°)	Rake (°)				
105.120	28.140	5	345	26	85	171	64	92			4.6	Kong LZ et al., (2024)
105.133	28.104	3.467	345	23.298	93.288				0.066	1.707	4.9	This Study
105.110	28.098	6.235				171	42.450	99.827	0.798	6.352	5.1	

4.2 Linear Inversion for Slip Distribution

To resolve the co-seismic slip distribution of the Xingwen Ms 4.9 earthquake, we employed a bounded least-squares inversion based on the Okada (1992) elastic half-space dislocation model. The geometric parameters of the two candidate seismogenic faults (east-dipping with a strike of 345° and west-dipping with a strike of 171°) were fixed according to the results of nonlinear inversion. Each fault plane was extended to intersect the surface in the dip direction, and its length was set to 10 km. The faults were discretized into rectangular dislocation elements (approximately $0.4 \text{ km} \times 1 \text{ km}$ for the 345° plane and $0.4 \text{ km} \times 0.9 \text{ km}$ for the 171° plane) to obtain detailed characterization of the subsurface slip pattern.

We computed Green's functions describing the relationship between slip on each fault element and the downsampled InSAR line-of-sight observations. The inversion was conducted using the bounded least squares method (Stark and Parker, 1995), with dip-slip constrained within 20 cm. To ensure solution stability and smoothness, a modified Laplacian smoothing operator (Jiang GY et al., 2013) was incorporated by introducing virtual observations. The optimal smoothing factor was determined by analyzing the trade-off curve between slip roughness and data misfit (Figures 4b, 4d), constrained by the statistical range reported in previous studies (Zhao YW et al., 2024).

The inversion results (Figure 4a and 4c) indicate that for the east-dipping nodal plane (strike 345°), the major slip occurred at depths of 2–4 km, peaking at approximately 11.5 cm at a depth of 2.9 km, corresponding to a seismic moment of $4.38 \times 10^{16} \text{ N}\cdot\text{m}$ (Mw 5.0). For the west-dipping plane (strike 171°), slip was mainly distributed at depths of 2–6 km, with a maximum of 7.7 cm at 3.2 km and a moment of $4.83 \times 10^{16} \text{ N}\cdot\text{m}$ (Mw 5.0). Both models show negligible shallow slip above 1 km, confirming that the event did not rupture the surface and was a blind earthquake. The forward

modeling results (Figure 5) demonstrate that both fault models successfully reproduce the observed co-seismic deformation patterns, with an average RMSE of 0.17 cm.

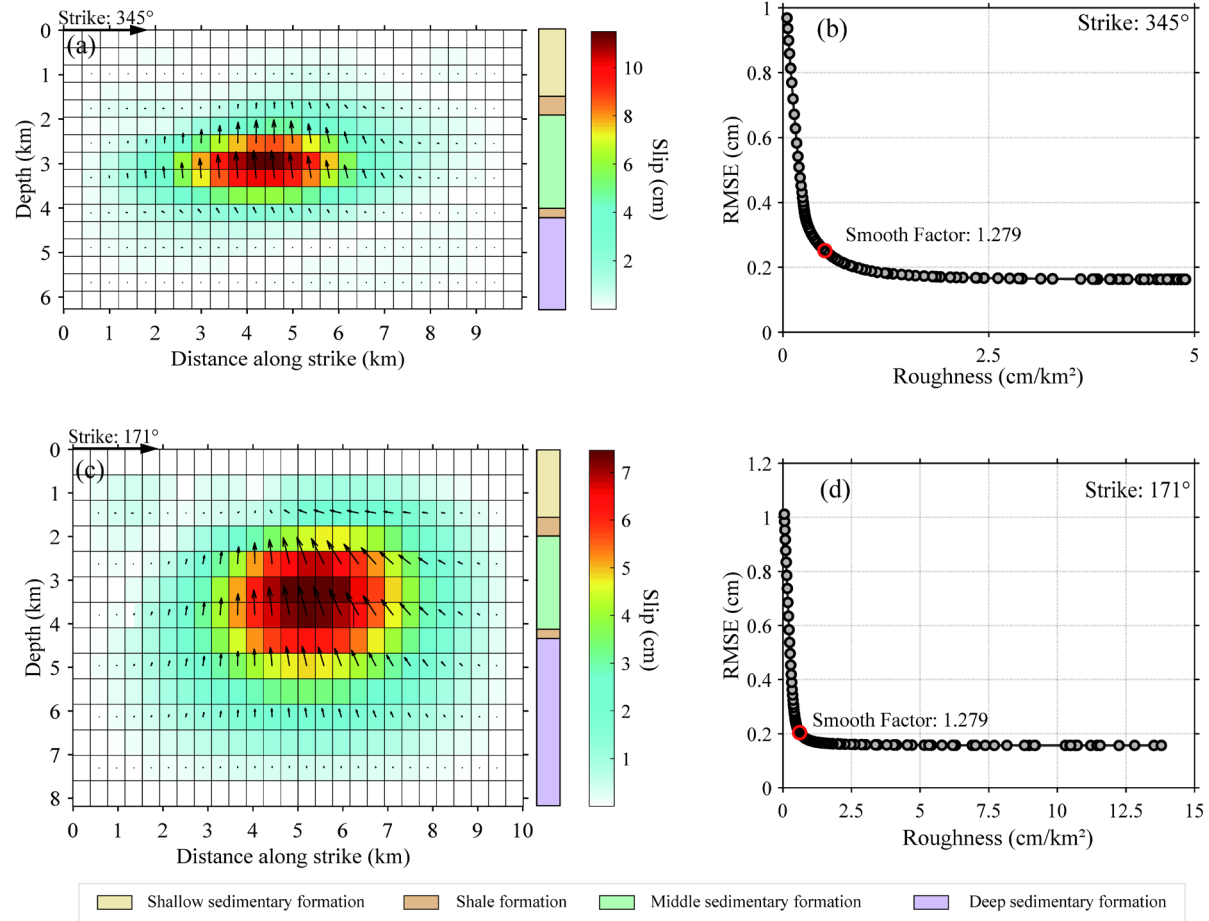


Figure 4. Inversion result of slip distribution and the trade-off curves between RMSE and roughness, with the final selected (optimized) smoothing factor annotated.

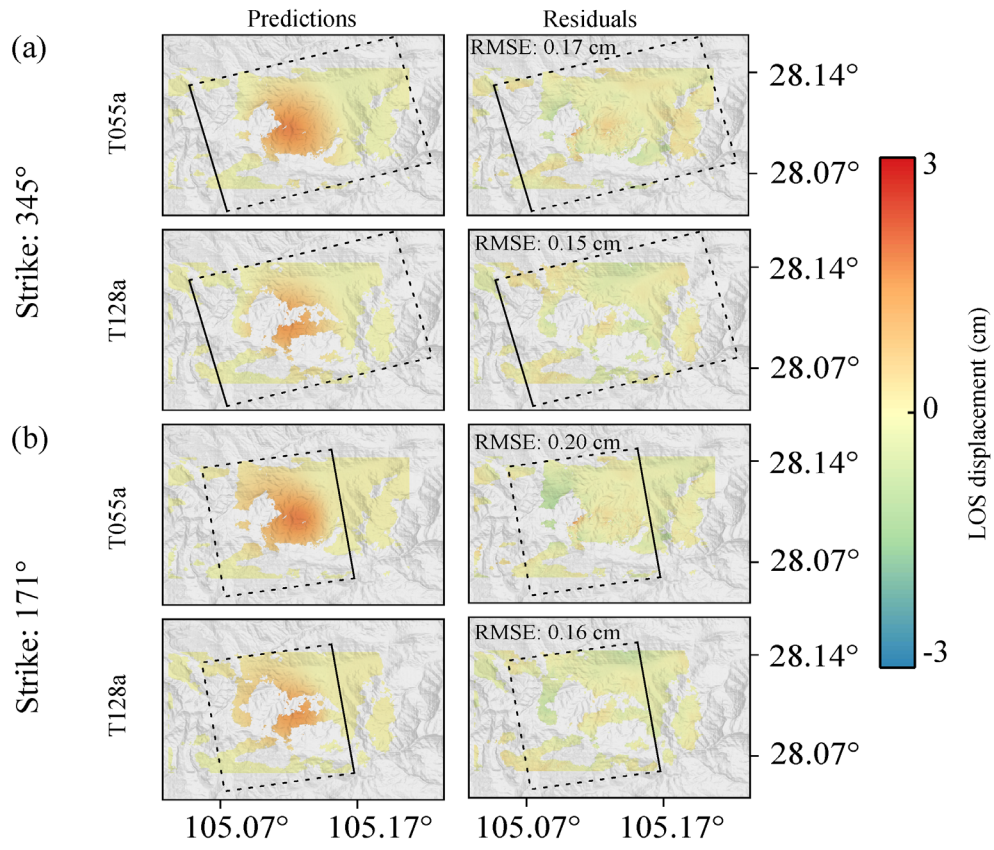


Figure 5. Forward result based on fault slip distribution model. (a) Forward result based on the fault with strike angle at 345° . (b) Forward result based on the fault with strike angle at 171° .

5 Relocation of earthquake sequence

As the nonlinear and linear inversion results cannot determine the source fault of the Ms 4.9 Xingwen earthquake, we further utilized high-precision aftershock relocation based on data from a pre-existing dense temporary seismic network in the epicentral area to better constrain the seismogenic structure. This network, originally deployed for regional microseismic monitoring, consisted of 48 short-period nodal seismometers (natural frequency \sim 5 Hz) equipped with 4G real-time transmission capability (Figure 1a). With an average station spacing of less than 10 km, it provided high-quality waveform data from July 1 2022 to July 31 2023, fully capturing the entire earthquake sequence.

We applied an established microseismic monitoring workflow to locate the earthquake sequence (Li JL et al., 2022; Yang W et al., 2023). The deep learning-based phase-picking algorithm PhaseNet was used to automatically detect P- and S-wave arrivals from continuous waveform data (Chen GY et al., 2023). Preliminary absolute locations were obtained using the open-source program NonLinLoc with a 3D velocity model constructed from ambient noise surface wave tomography (Li JL et al., 2022; Lomax et al., 2000). To further improve accuracy, the double-difference relocation method based on waveform cross-correlation differential times was applied (Waldhauser and Ellsworth 2000). Finally, a bootstrapping approach (Hillis and Bull 1993) involving 100 resampling iterations was performed to evaluate uncertainties and enhance the stability of the results.

The final relocation results show horizontal and vertical uncertainties of approximately 70 m and 100 m, respectively. A total of 5,789 seismic events were detected and relocated during the observation period (from July 1 2022 to July 31 2023), with magnitudes ranging from -0.5 to 4.9.

6 Discussion

To accurately determine the actual seismogenic fault plane, we combined temporal and spatial analyses of the aftershock sequence. The modified Omori's law (Utsu et al., 1961) was first applied to describe the temporal decay of aftershock activity and identify the appropriate time window for stable seismic behavior. Subsequently, Principal Component Analysis (PCA) (Wold et al., 1987) was employed to quantify the spatial pattern of the aftershock distribution and infer the dominant fault orientation from statistical geometry.

Fitting results from the modified Omori's law (Figure 6b) show that about 6.57 hours after the Ms 4.9 mainshock, aftershock activity had decreased to less than 15% of its maximum value. Therefore, aftershocks occurring within this time window were selected for further analysis. PCA was then conducted by constructing the covariance matrix of aftershock locations and performing eigenvalue decomposition to extract the principal axes of the distribution. The eigenvector associated with the largest eigenvalue defined the first principal component (A_1A_2), representing the dominant horizontal alignment of aftershocks, while the second component (B_1B_2), perpendicular to the first, was used to generate a vertical cross section for assessing dip geometry (Figure 1b).

The PCA results reveal that the dominant strike of the aftershock distribution (A_1A_2) aligns closely with the east-dipping nodal plane (strike 345°). The vertical section along B_1B_2 shows strong spatial consistency between the aftershock cluster and the east-dipping fault geometry (dip 23.3°), with most events concentrated near the slip centroid (~ 2.9 km depth). In contrast, the west-dipping nodal plane exhibits a clear mismatch with the aftershock pattern (Figure 6d). These results confirm that the east-dipping fault is the actual seismogenic plane, while the west-dipping plane can be excluded.

The relatively large inverted seismic moment (Mw 5.0) likely results from the cumulative deformation produced by four earthquakes with magnitudes greater than Ms 4.0 rather than by a single rupture. Both the main slip zone and the aftershock cluster are located beneath the shale production layer, mainly within sedimentary strata (Figure 4a 6c and 6d). Moreover, seismic activity (Figure 6a) intensified progressively within one month before the Ms 4.9 event, accelerating sharply during the week preceding the mainshock—suggesting potential influence from hydraulic fracturing operations in that period.

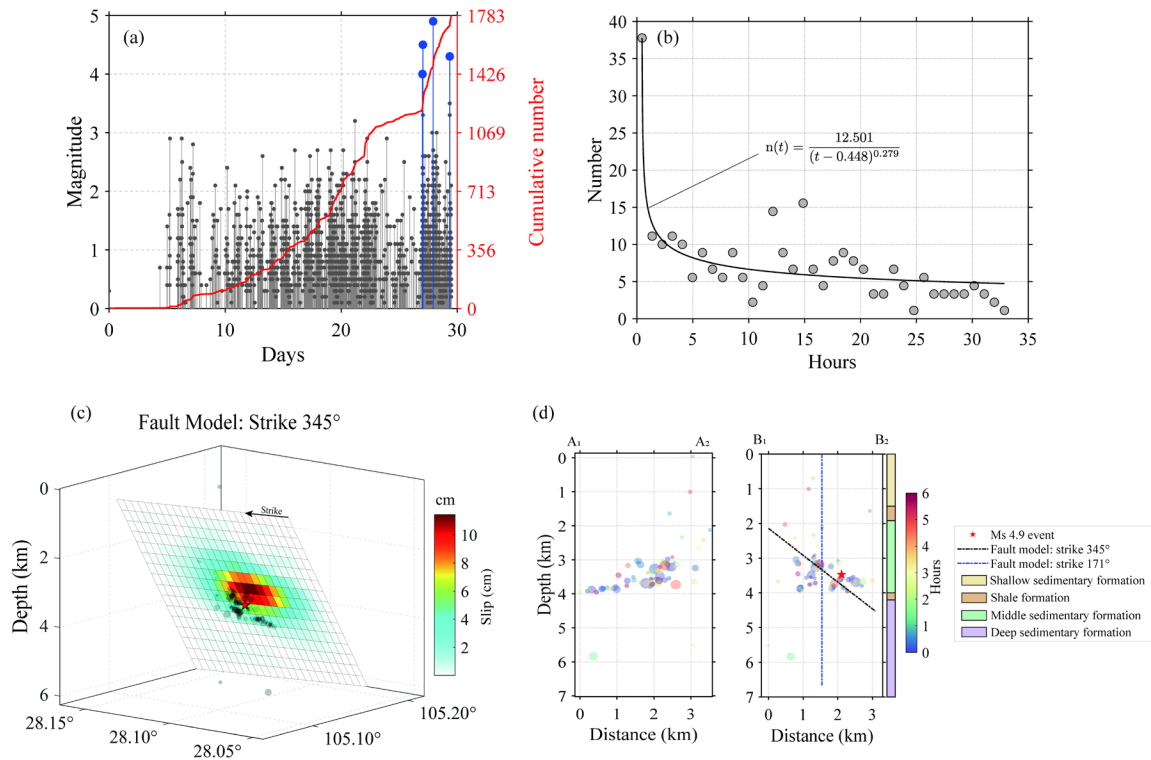


Figure 6. Analysis of the earthquake sequence relocation. (a) Temporal distribution of seismicity from April 6 2023 to May 6 2023 in Xinwen with $4 \text{ Ms} \geq 4$ events plotted in blue. (b) The decay histories of aftershock sequence of the Ms 4.9 earthquake and the fitting results (blue curves) with the modified Omori's law. (c) The 3-dimension slip distribution result. (d) The depth profile of A1A2 and B1B2 with strata according to the depth plotted. Currently, only the shallow shale formations is under production by systematic hydraulic stimulations with dense platforms (Li JL et l. 2023).

7 Conclusions

Based on Sentinel-1A SAR imagery from two ascending orbits, this study derived the co-seismic deformation field of the Ms4.9 Xingwen earthquake using D-InSAR technology, with multi-interferogram stacking applied to suppress noise. The deformation field exhibits thrust-dominated rupture characteristics, showing a maximum line-of-sight (LOS) displacement of approximately 3 cm. By integrating multi-start adaptive Gauss-Newton nonlinear inversion and bounded least-squares linear inversion, we accurately constrained the fault geometric parameters and slip distribution. The fault model was further validated through Principal Component Analysis (PCA) performed on dense seismic network locations of aftershocks.

The results indicate that the seismogenic structure is an east-dipping blind thrust fault with a strike of 345° and a dip angle of 23.3° . Slip is predominantly concentrated at depths between 2–4 km, peaking at approximately 2.9 km with a maximum slip of 11.5 cm. The estimated seismic moment is 4.38×10^{16} N·m, equivalent to a moment magnitude of Mw 5.0.

This study not only clarifies the rupture characteristics of the Ms4.9 earthquake but also demonstrates that geodetic methods can effectively complement seismological results in constraining source models. The well-determined fault model provides both a foundation and scientific support for understanding the earthquake's mechanism and conducting subsequent hazard assessments.

Acknowledgments, Samples, and Data

This work is supported by the National Natural Science Foundation (42130101, 42072245, 42204004, 42574012) of China. Sentinel-1 images are copyright of the European Space Agency and are freely available through the Copernicus Open Access Hub.

(<https://scihub.copernicus.eu/dhus/#/home>) or downloaded from Alaska Satellite Facility (<https://search.asf.alaska.edu/#/>).

Conflict of interest

The authors affirm that they have no financial and personal relationships with any individuals or organization that could have potentially influenced the work presented in this paper.

Chinese Abstract

2023年5月4日，四川省兴文县发生Ms 4.9级地震。尽管震级较小，但该事件对区域页岩气生产及周边居民生活构成了潜在威胁，并且其发震断层位置与破裂特征仍不明确。本文综合利用 InSAR 观测数据与地震精定位结果，反演确定了兴文地震的发震构造及破裂特征。基于两个升轨方向的 18 景 Sentinel-1A SAR 影像，研究采用 D-InSAR 方法提取同震形变，并通过多干涉图叠加有效抑制噪声。结果显示，该地震以逆冲为主，最大视线向形变约为 3 cm。利用多起点自适应 Gauss - Newton 非线性反演与有界最小二乘线性反演方法，获得了断层几何参数及滑动分布特征。结合主成分分析（PCA）得到的余震分布结果，识别出实际发震断层为一条倾向东的盲逆冲断层（走向 345°、倾角 23.3°），滑动主要集中在 2 - 4 km 深度，最大滑动出现在约 2.9 km 处。地震矩为 4.38×10^{16} N·m，对应矩震级 Mw 5.0。研究结果揭示了兴文地震的破裂机制，表明 InSAR 与地震学方法的联合应用能够有效识别发震断层，为页岩气区地震风险评估提供了科学支撑。

亮点：

1. 兴文地震引起了显著的同震地表形变，最大视线方向（LOS）位移约为 3 cm。
2. 高精度余震重定位结果表明，发震断层向东倾，倾角约为 23.3°。
3. 兴文地震的主要滑动集中在页岩气层以下，峰值滑动量达 11.5 cm。

References

- Chen GY, Yang W, Tan YY, Zhang HJ, Li JL. 2023. Automatic phase detection and arrival picking for microseismic events in hydraulic fracturing based on machine learning and array correlation. Chinese Journal of Geophysics (in Chinese), 66(4): 1558-1574, doi: 10.6038/cjg2022P0542
- Bender B (1983) Maximum likelihood estimation of b values for magnitude grouped data. Bulletin of the Seismological Society of America 73:831–851. <https://doi.org/10.1785/BSSA0730030831>
- Doin M-P, Lasserre C, Peltzer G, et al (2009) Corrections of stratified tropospheric delays in SAR interferometry: Validation with global atmospheric models. Journal of Applied Geophysics 69:35–50. <https://doi.org/10.1016/j.jappgeo.2009.03.010>
- Eyre TS, Samsonov S, Feng W, et al (2022) InSAR data reveal that the largest hydraulic fracturing-induced earthquake in Canada, to date, is a slow-slip event. Sci Rep 12:2043. <https://doi.org/10.1038/s41598-022-06129-3>

Hillis DM, Bull JJ (1993) An Empirical Test of Bootstrapping as a Method for Assessing Confidence in Phylogenetic Analysis. *Systematic Biology* 182–192

Jiang GY, Qiao XJ, Wang XQ, et al (2020) GPS observed horizontal ground extension at the Hutubi (China) underground gas storage facility and its application to geomechanical modeling for induced seismicity. *Earth and Planetary Science Letters* 530:115943. <https://doi.org/10.1016/j.epsl.2019.115943>

Jiang GY, Wen YM, Li K, et al (2018) A NE-Trending Oblique-Slip Fault Responsible for the 2016 Zaduo Earthquake (Qinghai, China) Revealed by InSAR Data. *Pure and Applied Geophysics* 175:4275–4288. <https://doi.org/10.1007/s00024-018-1948-0>

Jiang GY, Xu CJ, Wen YM, et al (2013) Inversion for coseismic slip distribution of the 2010 Mw 6.9 Yushu Earthquake from InSAR data using angular dislocations. *Geophysical Journal International* 194:1011–1022. <https://doi.org/10.1093/gji/ggt141>

Kijko A (1988) Maximum likelihood estimation of Gutenberg-Richter parameter for uncertain magnitude values. *PAGEOPH* 127:573–579. <https://doi.org/10.1007/BF00881745>

Kong LZ, Qi YP, Chen MD, Zhang Y (2024) Analysis on focal mechanism of sichuan xingwen ms4. 9 earthquake swarm in 2023. *PLATEAU EARTHQUAKE RESEARCH* 36:10–17

Li JL, Xu J, Zhang HJ, et al (2023) High seismic velocity structures control moderate to strong induced earthquake behaviors by shale gas development. *Commun Earth Environ* 4:188. <https://doi.org/10.1038/s43247-023-00854-x>

Li JL, Yao HJ, Wang BS, et al (2022) A real-time AI-assisted seismic monitoring system based on new nodal stations with 4G telemetry and its application in the Yangbi MS 6.4 aftershock monitoring in southwest China. *Earthquake Research Advances* 2:100033. <https://doi.org/10.1016/j.eqrea.2021.100033>

Liang SS, Zou LY, Liu YQ, Ren X (2024) Determination of focal mechanism solutions of the earthquakes with $M \geq 4.0$ occurred in the mainland of China during November 2023 to February 2024. *gjdzdt* 54:229–236. <https://doi.org/10.19987/j.dzkxjz.2024-036>

Lomax A, Virieux J, Volant P, Berge-Thierry C (2000) Probabilistic Earthquake Location in 3D and Layered Models

Luo H, Wang T, Wei SJ, et al (2021) Deriving Centimeter-Level Coseismic Deformation and Fault Geometries of Small-To-Moderate Earthquakes From Time-Series Sentinel-1 SAR Images. *Frontiers in Earth Science* 9:. <https://doi.org/10.3389/feart.2021.636398>

Miao SY, Zhang HJ, Gu N, et al (2024) Joint inversion of the rupture process of 2018 ML5. 7 Xingwen earthquake based on seismic and InSAR observations. *Seismology and Geology* 46:397–413

Okada Y (1992) Internal deformation due to shear and tensile faults in a half-space. *Bulletin of the Seismological Society of America* 82:1018–1040.

<https://doi.org/10.1785/BSSA0820021018>

Schultz R, Woo J, Pepin K, et al (2023) Disposal From In Situ Bitumen Recovery Induced the M_L 5.6 Peace River Earthquake. *Geophysical Research Letters* 50:e2023GL102940. <https://doi.org/10.1029/2023GL102940>

Stark PB, Parker RL Bounded-Variable Least-Squares: an Algorithm and Applications

Tian X, Liao MS (2013) The analysis of conditions for InSAR in the field of deformation monitoring. *Chinese Journal of Geophysics* 56:812–823. <https://doi.org/10.6038/cjg20130310>

Utsu, T. (1961), A statistical study on the occurrence of aftershocks, *Geophys. Mag.*, 30, 521–605.

Waldhauser F, Ellsworth WL (2000) A Double-Difference Earthquake Location Algorithm: Method and Application to the Northern Hayward Fault, California. *Bulletin of the Seismological Society of America* 90:1353–1368. <https://doi.org/10.1785/0120000006>

Wang S, Jiang GY, Lei XL, et al (2022) Three $M_w \geq 4.7$ Earthquakes Within the Changning (China) Shale Gas Field Ruptured Shallow Faults Intersecting With Hydraulic Fracturing Wells. *JGR Solid Earth* 127:e2021JB022946. <https://doi.org/10.1029/2021JB022946>

Wang S, Jiang GY, Weingarten M, Niu YF (2020b) InSAR Evidence Indicates a Link Between Fluid Injection for Salt Mining and the 2019 Changning (China) Earthquake Sequence. *Geophysical Research Letters* 47:e2020GL087603. <https://doi.org/10.1029/2020GL087603>

Werner C, Wegmüller U, Strozzi T, Wiesmann A (2000) GAMMA SAR AND INTERFEROMETRIC PROCESSING SOFTWARE

Wold S, Esbensen K, Geladi P (1987) Principal component analysis. *Chemometrics and Intelligent Laboratory Systems* 2:37–52. [https://doi.org/10.1016/0169-7439\(87\)80084-9](https://doi.org/10.1016/0169-7439(87)80084-9)

Yang W, Liu F, Liu F, et al (2023) Real-time microseismic monitoring based on deep learning and wireless transmission. *Progress in Geophysics* 38:1656–1672. <https://doi.org/10.6038/pg2023GG0436>

Zhao Y, Jiang G, He K, et al (2025) A Novel Method of Stacking InSAR Interferograms for Measuring Localized Earthquake Deformation. *IEEE Transactions on Geoscience and Remote Sensing* 63:1–13. <https://doi.org/10.1109/TGRS.2025.3569252>

Zhao Y, Jiang G, Lei X, et al (2023) The 2021 Ms 6.0 Luxian (China) Earthquake: Blind Reverse-Fault Rupture in Deep Sedimentary Formations Likely Induced by Pressure Perturbation From Hydraulic Fracturing. *Geophysical Research Letters* 50:e2023GL103209. <https://doi.org/10.1029/2023GL103209>

Zhao Y, Xu C (2020) Adaptive multistart Gauss–Newton approach for geodetic data inversion of earthquake source parameters. *J Geod* 94:17. <https://doi.org/10.1007/s00190-020-01353-z>

Zhao Y, Xu C, Wen Y (2024) Variance component adaptive estimation algorithm for coseismic slip distribution inversion using interferometric synthetic aperture radar data. *J Geod* 98:62.
<https://doi.org/10.1007/s00190-024-01866-x>